

Measurement of the Positive Muon Anomalous Magnetic Moment to 127 ppb

D. P. Aguillard,³³ T. Albahri,³⁰ D. Allspach,⁷ J. Annala,⁷ K. Badgley,⁷ S. Baeßler,³⁵ I. Bailey,^{16, a} L. Bailey,²⁷ E. Barlas-Yucel,^{28, b} T. Barrett,⁶ E. Barzi,⁷ F. Bedeschi,¹⁰ M. Berz,¹⁷ M. Bhattacharya,⁷ H. P. Binney,³⁶ P. Bloom,¹⁸ J. Bono,⁷ E. Bottalico,³⁰ T. Bowcock,³⁰ S. Braun,³⁶ M. Bressler,³² G. Cantatore,^{12, c} R. M. Carey,² B. C. K. Casey,⁷ D. Cauz,^{26, d} R. Chakraborty,²⁹ A. Chapelain,⁶ S. Chappa,⁷ S. Charity,³⁰ C. Chen,^{22, 21, e} M. Cheng,²⁸ R. Chislett,²⁷ Z. Chu,^{21, e} T. E. Chupp,³³ C. Claessens,³⁶ F. Confortini,^{9, f} M. E. Convery,⁷ S. Corrodi,¹ L. Cotrozzi,³⁰ J. D. Crnkovic,⁷ S. Dabagov,^{8, g} P. T. Debevec,²⁸ S. Di Falco,¹⁰ G. Di Sciascio,¹¹ S. Donati,^{10, h} B. Drendel,⁷ A. Driutti,^{10, 29} M. Eads,¹⁹ A. Edmonds,^{2, 37} J. Esquivel,⁷ M. Farooq,³³ R. Fatemi,²⁹ K. Ferraby,³⁰ C. Ferrari,^{10, i} M. Fertl,¹⁴ A. T. Fienberg,³⁶ A. Fioretti,^{10, i} D. Flay,³² S. B. Foster,^{29, 2} H. Friedsam,⁷ N. S. Froemming,¹⁹ C. Gabbanini,^{10, i} I. Gaines,⁷ S. Ganguly,⁷ J. George,^{32, j} L. K. Gibbons,⁶ A. Gioiosa,^{25, k} K. L. Giovanetti,¹³ P. Girotti,^{10, l} W. Gohn,²⁹ L. Goodenough,⁷ T. Gorringe,²⁹ J. Grange,³³ S. Grant,^{1, 27} F. Gray,²⁰ S. Haciomeroglu,^{5, m} T. Halewood-Leagas,³⁰ D. Hampai,⁸ F. Han,²⁹ J. Hempstead,³⁶ D. W. Hertzog,³⁶ G. Hesketh,²⁷ E. Hess,¹⁰ A. Hibbert,³⁰ Z. Hodge,³⁶ S. Y. Hoh,^{22, 21, e} K. W. Hong,³⁵ R. Hong,^{1, 29} T. Hu,^{22, 21, e} Y. Hu,^{21, e} M. Iacovacci,^{9, f} M. Incagli,¹⁰ S. Israel,^{2, 32} P. Kammel,³⁶ M. Kargiantoulakis,⁷ M. Karuza,^{12, n} J. Kaspar,³⁶ D. Kawall,³² L. Kelton,^{29, 23} A. Keshavarzi,³¹ D. S. Kessler,³² K. S. Khaw,^{22, 21, e} Z. Khechadoorian,⁶ B. Kiburg,⁷ M. Kiburg,^{7, 18} O. Kim,³⁴ N. Kinnaird,² E. Kraegeloh,³³ J. LaBounty,³⁶ K. R. Labe,⁶ M. Lancaster,³¹ S. Lee,⁵ B. Li,^{21, o} D. Li,^{21, p} L. Li,^{21, e} I. Logashenko,^{4, q} A. Lorente Campos,²⁹ Z. Lu,^{21, e} A. Lucà,⁷ G. Lukicov,²⁷ A. Lusiani,^{10, r} A. L. Lyon,⁷ B. MacCoy,³⁶ R. Madrak,⁷ K. Makino,¹⁷ S. Mastroianni,⁹ R. McCarthy,^{2, s} J. P. Miller,² S. Miozzi,¹¹ B. Mitra,³⁴ J. P. Morgan,⁷ W. M. Morse,³ J. Mott,⁷ A. Nath,^{9, f} J. K. Ng,^{22, 21, e} H. Nguyen,⁷ Y. Oksuzian,¹ Z. Omarov,^{15, 5} W. Osar,⁶ R. Osofsky,³⁶ S. Park,⁵ G. Paulettat,^{26, d} J. Peck,²⁹ G. M. Piacentino,^{25, k} R. N. Pilato,³⁰ K. T. Pitts,^{28, b} B. Plaster,²⁹ N. Pohlman,¹⁹ C. C. Polly,⁷ D. Počanić,³⁵ J. Price,³⁰ B. Quinn,³⁴ M. U. H. Qureshi,¹⁴ G. Rakness,⁷ S. Ramachandran,^{1, j} E. Ramberg,⁷ R. Reimann,¹⁴ B. L. Roberts,² D. L. Rubin,⁶ M. Sakurai,²⁷ L. Santi,^{†, 26, d} C. Schlesier,^{28, t} A. Schreckenberger,⁷ Y. K. Semertzidis,^{5, 15} M. Sorbara,^{11, u} J. Stapleton,⁷ D. Still,⁷ C. Stoughton,⁷ D. Stratakis,⁷ D. Stöckinger,²⁴ H. E. Swanson,³⁶ G. Sweetmore,³¹ D. A. Sweigart,⁶ M. J. Syphers,¹⁹ Y. Takeuchi,^{22, 21, e} D. A. Tarazona,⁶ T. Teubner,³⁰ A. E. Tewsley-Booth,^{29, 33} V. Tishchenko,³ N. H. Tran,^{2, v} W. Turner,³⁰ E. Valetov,¹⁷ D. Vasilkova,³⁰ G. Venanzoni,^{30, w} T. Walton,⁷ A. Weisskopf,¹⁷ L. Welty-Rieger,⁷ P. Winter,¹ Y. Wu,¹ B. Yu,³⁴ M. Yucel,⁷ E. Zaid,³⁰ Y. Zeng,^{22, 21, e} and C. Zhang³⁰

(The Muon $g - 2$ Collaboration)

¹Argonne National Laboratory, Lemont, Illinois, USA

²Boston University, Boston, Massachusetts, USA

³Brookhaven National Laboratory, Upton, New York, USA

⁴Budker Institute of Nuclear Physics, Novosibirsk, Russia

⁵Center for Axion and Precision Physics (CAPP) / Institute for Basic Science (IBS), Daejeon, Republic of Korea

⁶Cornell University, Ithaca, New York, USA

⁷Fermi National Accelerator Laboratory, Batavia, Illinois, USA

⁸INFN, Laboratori Nazionali di Frascati, Frascati, Italy

⁹INFN, Sezione di Napoli, Naples, Italy

¹⁰INFN, Sezione di Pisa, Pisa, Italy

¹¹INFN, Sezione di Roma Tor Vergata, Rome, Italy

¹²INFN, Sezione di Trieste, Trieste, Italy

¹³Department of Physics and Astronomy, James Madison University, Harrisonburg, Virginia, USA

¹⁴Institute of Physics and Cluster of Excellence PRISMA+,
Johannes Gutenberg University Mainz, Mainz, Germany

¹⁵Department of Physics, Korea Advanced Institute of Science and Technology (KAIST), Daejeon, Republic of Korea

¹⁶Lancaster University, Lancaster, United Kingdom

¹⁷Michigan State University, East Lansing, Michigan, USA

¹⁸North Central College, Naperville, Illinois, USA

¹⁹Northern Illinois University, DeKalb, Illinois, USA

²⁰Regis University, Denver, Colorado, USA

† Deceased.

²¹*School of Physics and Astronomy, Shanghai Jiao Tong University, Shanghai, China*
²²*Tsung-Dao Lee Institute, Shanghai Jiao Tong University, Shanghai, China*
²³*Department of Physics and Astronomy, Trinity University, San Antonio, Texas, USA*
²⁴*Institut für Kern- und Teilchenphysik, Technische Universität Dresden, Dresden, Germany*
²⁵*Università del Molise, Campobasso, Italy*
²⁶*Università di Udine, Udine, Italy*
²⁷*Department of Physics and Astronomy, University College London, London, United Kingdom*
²⁸*University of Illinois at Urbana-Champaign, Urbana, Illinois, USA*
²⁹*University of Kentucky, Lexington, Kentucky, USA*
³⁰*University of Liverpool, Liverpool, United Kingdom*
³¹*Department of Physics and Astronomy, University of Manchester, Manchester, United Kingdom*
³²*Department of Physics, University of Massachusetts, Amherst, Massachusetts, USA*
³³*University of Michigan, Ann Arbor, Michigan, USA*
³⁴*University of Mississippi, University, Mississippi, USA*
³⁵*University of Virginia, Charlottesville, Virginia, USA*
³⁶*University of Washington, Seattle, Washington, USA*
³⁷*City University of New York at York College, Jamaica, New York, USA*

(Dated: 12th June, 2025)

A new measurement of the magnetic anomaly a_μ of the positive muon is presented based on data taken from 2020 to 2023 by the Muon $g-2$ Experiment at Fermi National Accelerator Laboratory (FNAL). This dataset contains over 2.5 times the total statistics of our previous results. From the ratio of the precession frequencies for muons and protons in our storage ring magnetic field, together with precisely known ratios of fundamental constants, we determine $a_\mu = 116\,592\,0710(162) \times 10^{-12}$ (139 ppb) for the new datasets, and $a_\mu = 116\,592\,0705(148) \times 10^{-12}$ (127 ppb) when combined with our previous results. The new experimental world average, dominated by the measurements at FNAL, is $a_\mu(\text{exp}) = 116\,592\,0715(145) \times 10^{-12}$ (124 ppb). The measurements at FNAL have improved the precision on the world average by over a factor of four.

Introduction — Precise measurements of magnetic moments of charged leptons serve as precision probes of the Standard Model (SM) due to their sensitivity to particles and interactions within the SM and potentially Beyond the Standard Model (BSM). The Dirac equation [1] predicted $g_e \equiv 2$ for the g-factor g_e that relates the electron magnetic moment to its spin. Schwinger's radiative correction [2], inspired by contemporaneous experimental data [3, 4], refined this result and introduced the anomaly $a_e = \alpha/2\pi$. This work laid the foundation for modern relativistic field theory and the development of the SM.

The magnetic anomaly $a \equiv (g-2)/2$ ¹ arises from radiative corrections from virtual particles and can be calculated precisely within the SM. While a_e is measured [5] 1000 times more precisely than a_μ , the muon's greater mass makes a_μ about 4×10^4 times more sensitive to much BSM physics. Precision measurements of g_μ span decades of advances, beginning with early experiments at Columbia University Nevis Laboratory [6, 7] and the University of Liverpool [8]. Direct measurement of a_μ started with the CERN-I [9], CERN-II [10] and CERN-III experiments [11], which the Brookhaven National Laboratory (BNL) E821 experiment further improved [12]. The E821 results revealed a statistically significant tension with SM predictions at the time. The Muon $g-2$ Experiment at FNAL confirmed the E821 re-

sult with the 2018 Run-1 data [13], then refined a_μ with over twice the precision with the Run-2/3 data [14].

This paper presents a measurement of a_μ from the Muon $g-2$ Experiment using data collected in three runs spanning 2020 to 2023 (designated as Run-4, Run-5, and Run-6). The Run-4/5/6 positron statistics, over 2.5 times that of our previous measurements [13, 14], improve our final Run-1-6 statistical precision by more than 2.5. Our final result surpasses our original statistical and systematic goals [15] and establishes a stringent benchmark for future theoretical BSM extensions.

Experimental principle — Our Run-1 and Run-2/3 publications [13, 14, 16–19] detail the experiment. Polarized muon beams are injected into a 7.112 m radius storage ring with a design storage momentum of 3.1 GeV/c. A superconducting magnet generates a homogeneous vertical 1.45 T dipole field [20] that provides weak horizontal focusing of the beam and drives the muon spin precession. Two critical components for beam storage are a fast kicker that redirects muons onto the central orbit [21] and an electrostatic quadrupole (ESQ) system for vertical focusing [22]. At the design momentum, the contributions to the muon spin precession from the electric fields in the ESQ cancel.

The experiment determines the ratio of two frequencies, $\mathcal{R}'_\mu = \omega_a/\tilde{\omega}'_p(T_r)$, where ω_a is the difference between the spin precession and cyclotron frequencies of the muon, and $\tilde{\omega}'_p(T_r)$ is the nuclear magnetic resonance (NMR) precession frequency of shielded protons in a spherical water sample (corrected to a reference tempera-

¹ The magnetic anomaly a is often also called the anomalous magnetic moment.

ture T_r), averaged over the muon distribution, which expresses the magnetic field strength. The ω_a measurement utilizes 24 PbF₂ electromagnetic (EM) calorimeters [23–25] that record the energy and time of incident positrons. Parity violation in muon decay and the Lorentz boost of the beam couple to provide an oscillation in the rate of high-energy positrons at a frequency of ω_a . A laser system [26] continuously monitors the gain of each crystal in the calorimeters. A chain of magnetic field measurements yields $\tilde{\omega}'_p(T_r)$, where the tilde indicates muon-weighted averaging. The chain begins with a periodic mapping of the magnetic field by a movable mapper with 17 NMR probes [27]. These probes are calibrated *in-situ* against a water-based cylindrical probe that transfers the absolute calibration of shielded protons in a spherical water sample [28]. Additional NMR probes [29], embedded in the experiment’s vacuum chambers, track the field while muons are stored between mappings. The mapped and tracked magnetic field is weighted by the muon distribution, M , measured using two straw tracker stations [30].

The narrow aperture through which the beam enters the storage ring produces a mismatch between the phase space of the incoming beam and the storage ring acceptance that leads to coherent betatron oscillation (CBO). This coherent beam motion introduces a time variation into the positron detection efficiency. After Run-4, an additional RF system [31] added a small modulation of the ESQ high voltage during the first 6 μs after muon injection. The RF system generates dipole fields tuned to the CBO frequency, resonantly damping the CBO by applying forces out of phase. For analysis purposes, the data is divided into four distinct datasets based on RF configurations: noRF (no RF system), xRF (horizontal RF fields only), and xyRF5/xyRF6 (both horizontal and vertical RF fields in Run-5 and Run-6, respectively).

The measured anomalous spin frequency, ω_a^m , and the muon-weighted magnetic field, $\langle \omega'_p \times M \rangle$, must be corrected for several effects via

$$\mathcal{R}'_\mu = \frac{\omega_a^m (1 + C_e + C_p + C_{pa} + C_{dd} + C_{ml})}{\langle \omega'_p(T_r) \times M \rangle (1 + B_k + B_q)}, \quad (1)$$

collectively shifting \mathcal{R}'_μ by 572 ppb (see Tab. I). The corrections to ω_a^m address: the residual contribution to the muon spin precession rate from electric fields C_e ; the contribution to the muon spin precession from the vertical betatron motion C_p ; time-dependent changes in the mean phase of the observed muon ensemble caused by (i) detector acceptance C_{pa} , and by phase-momentum correlations coupled to (ii) momentum-dependent muon lifetimes C_{dd} and (iii) momentum-dependent muon storage losses C_{ml} . Corrections to the muon-weighted magnetic field accommodate the fast transient fields not captured in the NMR-based field maps, specifically from eddy currents generated by the fast injection kickers B_k and from vibrations of the ESQ plates B_q , both synchronous with muon injection. Table I summarizes the corrections.

Quantity	Correction (ppb)	Uncertainty (ppb)
ω_a^m (statistical)	...	114
ω_a^m (systematic)	...	30
C_e	347	27
C_p	175	9
C_{pa}	-33	15
C_{dd}	26	27
C_{ml}	0	2
$\langle \omega'_p \times M \rangle$ (mapping, tracking)	...	34
$\langle \omega'_p \times M \rangle$ (calibration)	...	34
B_k	-37	22
B_q	-21	20
μ'_p/μ_B	...	4
m_μ/m_e	...	22
Total systematic for \mathcal{R}'_μ	...	76
Total for a_μ	572	139

TABLE I. Values and uncertainties of the \mathcal{R}'_μ terms in Eq. (1), and uncertainties due to the external parameters in Eq. (2) for a_μ . The $\langle \omega'_p \times M \rangle$ uncertainties are separated into mapping and calibration contributions.

From $\mathcal{R}'_\mu = \omega_a/\tilde{\omega}'_p(T_r)$, we determine a_μ via:

$$a_\mu = \frac{\omega_a}{\tilde{\omega}'_p(T_r)} \frac{\mu'_p(T_r)}{\mu_B} \frac{m_\mu}{m_e}, \quad (2)$$

where $\mu'_p(T_r)/\mu_B$ is the ratio of the shielded proton magnetic moment to the Bohr magneton at $T_r = 25^\circ\text{C}$ and m_μ/m_e is the muon-to-electron mass ratio ².

Anomalous precession frequency ω_a^m —Reconstruction of either individual positron candidates or the total calorimeter energy from the digitized EM calorimeter waveforms provides the oscillating time series that get fit to determine ω_a^m . Four independent analysis groups utilize three different positron reconstruction and pileup correction algorithms while a fifth group performs energy reconstruction [16, 19]. The positron reconstructions have nonlinear energy differences due to the treatment of low energy crystals, differ in the level of unresolved overlapping positrons (pileup) by up to an order of magnitude, and differ in the positron content by several percent. Consistency of the ω_a^m values from these algorithms speaks to the robustness of the measurement.

Each positron-based analysis constructs its time series using one of three methods [16, 19]. The first method bins the positron time directly. The second subdivides the data to construct a ratio that isolates the oscillation from the exponential decay and reduces sensitivity to slow response changes. A new method fits for ω_a^m in slices of the dominant horizontal CBO phase to reduce sensitivity to CBO. Parity violation in muon decay manifests

² $\mu'_p/\mu_B = 1.520\,993\,155\,1(62) \times 10^{-3}$;
 $m_\mu/m_e = 206.768\,2827(46)$, both from [32].

as an energy-dependent amplitude, or asymmetry, $A(E_e)$ in the ω_a^m oscillation. Weighting each positron by $A(E_e)$ maximizes the statistical power [33]. The five groups provide seven asymmetry-weighted results for $E_e > 1.0$ GeV whose simple average (assuming full correlation) gives ω_a^m . Two energy-based and 11 unit-weighted measurements for $E_e > 1.7$ GeV provide 13 crosschecks.

Each group fits their time series using one of two models. The first, used previously, takes the form

$$N(t) = N_0 \Lambda(t) \eta_N(t) e^{-t/\gamma\tau_\mu} \times \{1 + A \eta_A(t) \cos[\omega_a^m t - \varphi_0 + \eta_\phi(t)]\}, \quad (3)$$

where N_0 is the normalization, $\gamma\tau_\mu$ is the average boosted muon lifetime (≈ 64.4 μ s), $\Lambda(t)$ accounts for beam loss, A is the average rate asymmetry, and $-\varphi_0$ is the average phase extrapolated to $t = 0$. The factors η_N , η_A , and η_ϕ are well-motivated corrections that accommodate the rate variations from the coupling of calorimeter acceptance with beam oscillations, whose frequencies can be seen in Figure 1. A second, complementary model replaces those factors with a sum $\sum_i \xi_i(t)$ over those frequencies that modulate the $\{1 + A \cos(\omega_a^m t - \varphi_0)\}$ precession term. The fits begin near 30 μ s to allow the ESQ fields, and thus the muon beam, to stabilize.

Each analysis group developed its analysis using an unknown, fixed, pseudorandom offset in the precession frequency. These blindings add to the hardware blinding of the digitization frequency, which was set and monitored by FNAL physicists outside the collaboration. Shortly before the hardware unblinding, the groups shifted to a common unknown blind and two of the seven analyses included in the final average addressed minor issues in the $\eta_\phi(t)$ treatment exposed by the comparisons, with changes on the scale of a few parts per billion (ppb). Removal of the hardware blinding occurred after all aspects of the a_μ determination were complete and frozen.

All fits model the data well, and meet the requirement for inclusion in the final result: a good χ^2 and a Fourier transform of the fit residuals free of artifacts, as illustrated for the combined data in Fig. 1. The fit for the highest statistics dataset has a χ^2 of 4007 for 4097 degrees of freedom, and a probability of χ^2 of 84%. Fits in positron energy bins, individual calorimeter stations, and as a function of fit start and end time show only statistical scatter in ω_a^m . The twenty correlated ω_a^m values agreed within the allowed statistical variations assessed using 200 bootstrap samples. The ω_a^m statistical uncertainty of 114 ppb dominates the Run-4/5/6 a_μ uncertainty.

Uncertainties in the envelopes of the transverse beam oscillations and in a new correction for an intensity-dependent calorimeter gain sag dominate the systematic uncertainties, each contributing at the level of 25-40 ppb in the four fit datasets. The gain sag largely explains a residual slow term observed in the data in the previous publications [16, 19] (in addition to a small issue in one

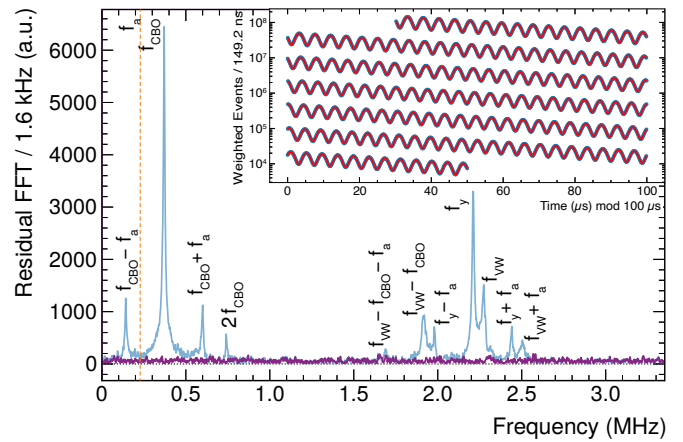


FIG. 1. Fourier transform of the residuals from the sum of the four fits to the Run-4/5/6 data excluding (blue) and including (purple) the $\xi(i)$ terms that incorporate the beam oscillation effects. The peaks correspond to the betatron frequencies (see [16] for frequency definitions). The RF-driven CBO damping has decreased the power at f_{CBO} compared to earlier data. The dashed line (orange) indicates the anomalous precession frequency f_a . Inset: the asymmetry-weighted e^+ time spectrum for the summed data (blue) and fit functions (red).

of the reconstructions that has been corrected here), and has been well-measured with dedicated laser studies using a full calorimeter station. While the magnitude of the sag is below our design specification, it oscillates at ω_a^m with a phase shift relative to the beam intensity, creating a greater ω_a^m sensitivity than previously estimated.

Beam-dynamics corrections C_i — The leading correction C_e to ω_a^m derives from the measured muon momentum distribution, which has about a 0.1% relative width. The debunching of the muon beam that results from the spread of cyclotron frequencies can be observed in calorimeter data at early times in a muon fill. That data determines the momentum distribution of the stored muons and the correlation between momentum and relative time in the bunch [18, 19]. The reconstructed radial muon distribution from the trackers also determines that information. Both methods were cross-checked with a minimally-intrusive, insertable scintillating fiber detector in dedicated studies, a novelty of this dataset. The staged introduction of the ESQ RF reduced the size of this correction from 387 ppb to 318 ppb–382 ppb. The improved understanding and enhanced robustness of these methods reduced the uncertainty from 32 ppb in Run-2/3 to 27 ppb in Run-4/5/6.

The tracker data provide the distribution of the stored muons' vertical betatron amplitudes, which lead to the correction C_p . The analysis method remains unchanged from the Run-1 [18] and Run-2/3 [19] analyses.

As the muon beam evolves, changes in the distribution of muons whose daughter positron has been detected can lead to a time-dependent change in the ensemble-

averaged spin precession phase, which causes bias in ω_a^m . The calorimeter acceptance and relative phase versus transverse decay position are evaluated through simulation. Combining these with the transverse beam distribution measured in the trackers provides the C_{pa} correction. The method, resulting values, and uncertainty remain consistent with the Run-2/3 evaluation.

Correlations between the muon phase and its momentum, together with the momentum dependence of its lifetime, lead to the differential decay correction C_{dd} . Phase-momentum correlations in the stored muon ensemble originate from the upstream beamline and the injection process. These effects are evaluated in simulation and supported by dedicated measurements in which the momentum acceptance of the storage ring is changed. Another contribution arises from correlations of injection time and momentum – early muons spend additional time in the storage ring field compared to late ones, so build up a relative precession phase shift. The temporal shape of the kicker pulse and the relative timing between kicker pulse and muon injection dominate those correlations. This contribution is evaluated from the momentum-injection time distributions from calorimeter data that were used to calculate C_e . These kicker-related contributions vary over a range of ± 50 ppb for different time periods and for the muon bunch position in the 16-bunch cycle. Cancellations in averaging lead to 4 ppb–8 ppb corrections to the main datasets with uncertainties of 17 ppb–19 ppb.

Lastly, time-dependent phase changes can be caused by muon loss. Loss rates have been significantly reduced compared to earlier runs by optimizing storage conditions. The introduction of RF decreased these losses further, leaving a negligibly small correction, C_{ml} .

Muon-weighted magnetic field $\langle \omega'_p \times M \rangle$ — The determination of the muon-weighted magnetic field largely follows the procedure developed earlier [17, 19]. The magnetic field showed azimuthal variations with an RMS below 20 ppm. The relative field change over the muon storage radius of 45 mm caused by azimuthally-averaged transverse linear and higher-order gradients is below 100 ppb and 1 ppm, respectively. Figure 2 superimposes the azimuthally averaged magnetic field contour lines from the xyRF5 dataset on the time- and azimuthally averaged muon distribution.

The Run-4/5/6 dataset spans 194 magnetic field maps, compared with 16 in Run-1 and 69 for Run-2/3. All but four of the azimuthally averaged magnetic maps field stayed within a range of ± 1.3 ppm. The remainder, still included in this work, exhibited variations up to 10 ppm.

The uncertainty in the field maps for Run-4/5/6 reduced to 29 ppb–31 ppb compared to 37 ppb–39 ppb in Run-2/3, primarily due to additional measurements of the magnetic footprint of the field mapper’s parking mechanism. Its uncertainty contribution dropped from 22 ppb to 2 ppb, but these map uncertainty gains are

partially offset by the larger temperature differences between the NMR probes during magnetic field mapping and during their *in-situ* calibration, increasing the uncertainty from the NMR probe temperature dependence from 9 ppb–15 ppb to 13 ppb–16 ppb.

The increased number of tracked magnetic field maps compared to our previous publications allowed for more detailed studies of systematic effects in that tracking, particularly of local drifts at magnet pole edges as a function of time after a magnet ramp-up. The remaining systematic uncertainty is evaluated using a Brownian bridge model and a new time-independent constant model, which yielded similar results. The associated total tracking uncertainty reduced to 8 ppb–14 ppb from 17 ppb–18 ppb due to the larger number of magnetic field maps. The muon weighting, which adjusts the field maps for the field experienced on average by the stored muons, follows our previous approach, yielding uncertainties of 6 ppb–7 ppb comparable to those of Run-3b which had similar muon distributions.

Two analysis teams with separate codebases performed the magnetic field map extraction, tracking, and weighting processes while software blinded. Their results were consistent. The uncertainties of magnetic field mapping, tracking and muon weighting combine for a total of 33 ppb–35 ppb by dataset and 34 ppb in the final average.

In-situ calibrations of the field mapper NMR probes were performed before and after each of the three Run-4/5/6 running periods ³. No time dependence was observed over the six years of data-taking, and the probe calibrations are averaged, contributing an uncertainty of 16 ppb. Since the same calibration probe was used in Run-2/3, the absolute calibration with respect to shielded protons in a spherical water sample remains unchanged. Additional work enhanced our understanding of the material effects of the calibration probe but had no direct impact on the associated 8 ppb uncertainty.

The absolute calibration was cross-checked against ³He-based magnetometers [34], which showed a 1.7 standard deviation difference. Comparisons to water-based continuous-wave NMR probes developed by the J-PARC Muon $g - 2$ /EDM collaboration [35] showed inconsistencies in early comparisons but good agreement in later iterations. These new crosschecks lead to an additional 25 ppb uncertainty, resulting in a total calibration uncertainty of 34 ppb.

The total systematic uncertainty of the muon-weighted magnetic field, including calibration, increased by 10 ppb to a total of 48 ppb with respect to Run-2/3, primarily driven by the uncertainties on the absolute calibration.

Magnetic field transients B_i — The time-dependent residual magnetic fields from eddy currents induced by

³ The calibration after Run-6 is only used as a cross-check and doesn’t enter the average.

the fast kicker magnets were measured *in-situ* with two independent magnetometers, both based on Faraday rotation in terbium gallium garnet crystals. One system uses optical fibers to guide the laser light into the kicker region. The second new system uses an open laser beam, which enters the storage volume through a window, and mirrors to guide the light. Two of the three kickers were measured at several transverse positions. The measurements from the two apparatus agree within uncertainties. Measurements at a large radius (18 mm) revealed transverse variations of about a factor of two, which were investigated with additional measurements on a mock-up. While the measurements close to the beam center are consistent with earlier determinations, the new measurements at a larger radial offset, together with improved understanding of the transverse modeling of the resulting field perturbation, lead to a larger correction term B_k than reported in Run-2/3. Driven by the observed stronger transverse variation of the transient and uncertainties in the transverse modeling, the total uncertainty increased to 22 ppb compared to Run-2/3.

The correction presented in reference [19] for magnetic field transients from vibrations in the ESQ system, B_q , remains valid. The transverse distribution of this effect was studied in more detail, and the assigned uncertainties were corroborated.

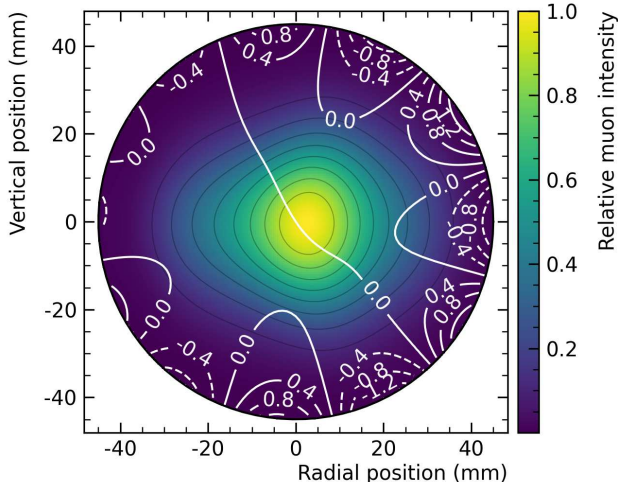


FIG. 2. Azimuthally averaged magnetic field contours in units of ppm overlaid in white on the time- and azimuthally averaged muon distribution for the xyRF5 dataset.

Calculation of a_μ — The values of ω_a and $\tilde{\omega}'_p$ listed in Tab. II for the four fit datasets, along with the corrections from Eq. (1), form \mathcal{R}'_μ . The \mathcal{R}'_μ measurements are statistically uncorrelated, while nearly all systematic uncertainties are fully correlated. The table also lists the combined Run-4/5/6 result and our earlier results, corrected as noted below. The four fit datasets show good consistency with a $\chi^2 = 0.96$ for 3 degrees of freedom, which has a probability of 80 %. No statistically signif-

icant correlations with magnet current, magnetic field, field gradients, or time of day were observed.

We report \mathcal{R}'_μ at $T_r = 25^\circ\text{C}$. This change from the reference temperature used in previous publications aligns with both the CODATA standard and our actual measurement conditions. Our previous \mathcal{R}'_μ values were adjusted by -101 ppb to reflect this change in reference temperature and external constants. The a_μ values do not change as a result of the T_r shift, though the external CODATA constants have been updated.

The superior statistical power of this larger dataset, along with additional dedicated measurements, enabled further cross-checks of the Run-2/3 results. Three corrections with corresponding uncertainty adjustments were identified and applied when combined with the latest dataset: the sensitivity of ω_a to small, slow gain shifts noted earlier, improved understanding of spatial dependencies in the transient magnetic fields from kicker system eddy currents, and a sign error correction in one component of the C_{dd} correction. These corrections, determined independently, happened to have the same sign and combine to shift the Run-1 and Run-2/3 results by 50 ppb and 98 ppb, respectively, and result in a total systematic uncertainty of 78 ppb for the adjusted Run-2/3 result. The corrections were finalized before unblinding the Run-4/5/6 results. The latest result agrees well with the previous measurements.

The combined FNAL average, Run-1-6, with a total uncertainty of 127 ppb, assumes fully correlated systematic uncertainties between the results.

Following Eq. 2, we determine the muon anomaly $a_\mu(\text{Run-4/5/6}) = 116\,592\,0710(162) \times 10^{-12}$ (139 ppb)

$a_\mu(\text{Run-1-6}) = 116\,592\,0705(148) \times 10^{-12}$ (127 ppb),

for the full dataset, with the statistical, systematic, and external parameter uncertainties combined in quadrature. The combined experimental (exp) average, from BNL E821⁴ and Run-1-6, becomes

$a_\mu(\text{exp}) = 116\,592\,0715(145) \times 10^{-12}$ (124 ppb).

Figure 3 shows the corresponding values.

The Muon $g-2$ Theory Initiative has released an updated SM value of a_μ in their 2025 White Paper (WP2025) [36], based on results from [5, 37–95], which agrees with the measured average. The value shifts considerably compared to their 2020 White Paper (WP2020) [96], which is almost entirely due to the exclusive use of new, published leading-order hadronic vacuum polarization estimates based on lattice-QCD calculations. The previous value in their WP2020 used experimental $e^+e^- \rightarrow \text{hadrons}$ cross-section measurements from multiple experiments to evaluate this contribution based on

⁴ The adjusted $\mathcal{R}'_\mu(\text{BNL}) = 0.00370730154(172)_{\text{stat.}}(102)_{\text{syst.}}$ contributes 5.1 % to the new experimental average.

	$[\omega_a/2\pi - 229\,077] \text{ (Hz)}$	$[\tilde{\omega}'_p/2\pi - 61\,790\,900] \text{ (Hz)}$	$[\mathcal{R}'_\mu \times 10^{11} - 370\,730\,000]$
Run-1	25(161)(59)
Run-2/3	87(75)(29)
noRF	0.504(42)(12)	20.0(0.5)(3.5)	43(68)(29)
xRF	0.626(55)(11)	38.9(0.7)(3.4)	126(90)(28)
xyRF5	0.500(56)(12)	10.9(0.7)(3.4)	90(91)(28)
xyRF6	0.509(64)(11)	03.6(0.9)(3.5)	148(103)(28)
Run-4/5/6	90(42)(28)
Run-1-6	88(36)(29)

TABLE II. Measurements of ω_a , $\tilde{\omega}'_p$, and their ratios \mathcal{R}'_μ , with $\omega_a/2\pi$ and $\tilde{\omega}'_p/2\pi$ values shown as offsets from +229 077 Hz and +61 790 900 Hz, respectively, and $\mathcal{R}'_\mu \times 10^{11}$ values as offsets from 370 730 000. The Run-1 and Run-2/3 values have been updated from [14] as described in the text. The uncertainties are shown in the form $(\text{stat.}) (\text{syst.})$.

a dispersion integral and showed a discrepancy with the experimental value. However, a recent cross-section measurement [97, 98] has increased the tension among the experimental inputs, thus a prediction based on the dispersion integral was not included in their WP2025. Efforts are continuing towards an evaluation of this leading-order hadronic contribution using both lattice-QCD and dispersion integral calculations.

In summary, we report the measurement of the muon magnetic anomaly to a precision of 127 ppb using our full six years of data. With over a four-fold improvement in precision over the BNL E821 measurement [12], this result represents the most precise determination of the muon magnetic anomaly and provides a powerful benchmark for extensions of the SM.

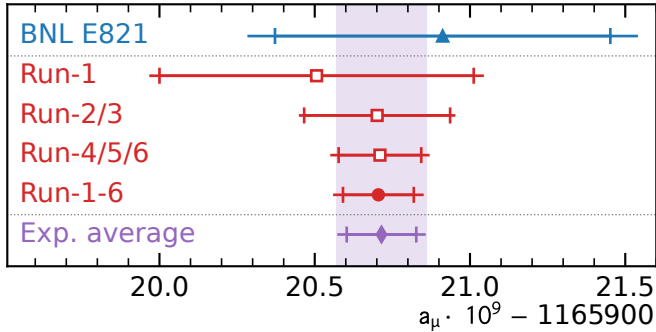


FIG. 3. Experimental values of a_μ from BNL E821 [12] (blue triangle), our Run-1 [13], Run-2/3 [14] and Run-4/5/6 (red squares), those three results combined (red circle), and the new experimental world average (purple diamond). The inner tick marks indicate the statistical contribution to the total uncertainties. Corrections to earlier results have been applied.

We thank the Fermilab management and staff for their strong support of this experiment, as well as our university and national laboratory engineers, technicians, and workshops for their tremendous support. Greg Bock, Joe

Lykken, and Rick Ford set the blinding clock and diligently monitored its stability. We also thank members of the J-PARC Muon $g-2$ /EDM experiment for the cross-calibration efforts.

The Muon $g-2$ Experiment was performed at the Fermi National Accelerator Laboratory, a U.S. Department of Energy, Office of Science, HEP User Facility. Fermilab is managed by Fermi Forward Discovery Group, LLC, acting under Contract No. 89243024CSC000002. Additional support for the experiment was provided by the U.S. DOE Office of Science under the offices of HEP, NP, ASCR, and the U.S.-Japan Science and Technology Cooperation Program in HEP, the U.S. National Science Foundation, the Istituto Nazionale di Fisica Nucleare (Italy), the Science and Technology Facilities Council (UK), the Royal Society (UK), the National Natural Science Foundation of China (Grant No. 12475108, 12305217, 12075151), MSIP, NRF, and IBS-R017-D1 (Republic of Korea), the Deutsche Forschungsgemeinschaft (DFG, German Research Foundation, Germany) through the Cluster of Excellence PRISMA+ (EXC 2118/1, Project ID 39083149), the European Union Horizon 2020 research and innovation programme under the Marie Skłodowska-Curie Grant Agreements No. 101006726 and No. 734303, the European Union STRONG 2020 project under Grant Agreement No. 824093, and the Leverhulme Trust, LIP-2021-014.

^a Also at The Cockcroft Institute of Accelerator Science and Technology, Daresbury, United Kingdom.

^b Now at Virginia Tech, Blacksburg, Virginia, USA.

^c Also at Università di Trieste, Trieste, Italy.

^d Also at INFN Gruppo Collegato di Udine, Sezione di Trieste, Udine, Italy.

^e Also at State Key Laboratory of Dark Matter Physics, Shanghai, China; also at Key Laboratory for Particle Astrophysics and Cosmology (MOE); also at Shanghai Key Laboratory for Particle Physics and Cosmology, Shanghai, China.

^f Also at Università di Napoli, Naples, Italy.

^g Also at Lebedev Physical Institute and NRNU MEPhI, Moscow, Russia.

^h Also at Università di Pisa, Pisa, Italy.

ⁱ Also at Istituto Nazionale di Ottica - Consiglio Nazionale delle Ricerche, Pisa, Italy.

^j Now at Alliance University, Bangalore, India.

^k Also at INFN, Sezione di Roma Tor Vergata, Rome, Italy.

^l Now at INFN, Laboratori Nazionali di Frascati, Frascati, Italy.

^m Now at İstinye University, Istanbul, Türkiye.

ⁿ Also at University of Rijeka, Rijeka, Croatia.

^o Also at Zhejiang Lab, Hangzhou, Zhejiang, China.

^p Also at Shenzhen Technology University, Shenzhen, Guangdong, China.

^q Also at Novosibirsk State University, Novosibirsk, Russia.

^r Also at Scuola Normale Superiore, Pisa, Italy.

^s Also at Northeastern University, Boston, Massachusetts, USA.

^t Now at Cornell University, Ithaca, New York, USA.

^u Also at Università di Roma Tor Vergata, Rome, Italy.

^v Now at Institute for Interdisciplinary Research in Science and Education (ICISE), Quy Nhon, Binh Dinh, Vietnam.

^w Also at INFN, Sezione di Pisa, Pisa, Italy.

[1] P. A. M. Dirac, The quantum theory of the Electron. Part II, *Proc. R. Soc. A* **118**, 351 (1928).

[2] J. S. Schwinger, On quantum electrodynamics and the magnetic moment of the electron, *Phys. Rev.* **73**, 416 (1948).

[3] P. Kusch and H. M. Foley, Precision measurement of the ratio of the atomic ‘*g* values’ in the $^2p_{\frac{3}{2}}$ and $^2p_{\frac{1}{2}}$ states of gallium, *Phys. Rev.* **72**, 1256 (1947).

[4] P. Kusch and H. M. Foley, The magnetic moment of the electron, *Phys. Rev.* **74**, 250 (1948).

[5] X. Fan, T. G. Myers, B. A. D. Sukra, and G. Gabrielse, Measurement of the Electron Magnetic Moment, *Phys. Rev. Lett.* **130**, 071801 (2023), arXiv:2209.13084 [physics.atom-ph].

[6] T. Coffin, R. L. Garwin, S. Penman, L. M. Lederman, and A. M. Sachs, Magnetic moment of the free muon, *Phys. Rev.* **109**, 973 (1958).

[7] R. L. Garwin, D. P. Hutchinson, S. Penman, and G. Shapiro, Accurate determination of the μ^+ magnetic moment, *Phys. Rev.* **118**, 271 (1960).

[8] J. M. Cassels, T. W. O’Keeffe, M. Rigby, A. M. Wetherell, and J. R. Wormald, Experiments with a polarized muon beam, *Proceedings of the Physical Society. Section A* **70**, 543 (1957).

[9] G. Charpak, F. J. M. Farley, R. L. Garwin, T. Muller, J. C. Sens, and A. Zichichi, The anomalous magnetic moment of the muon: a world average value, *Nuovo Cimento* **37**, 1241 (1965).

[10] J. Bailey, W. Bartl, G. Von Bochmann, R. Brown, F. Farley, H. Jöstlein, E. Picasso, and R. Williams, Precision measurement of the anomalous magnetic moment of the muon, *Physics Letters B* **28**, 287 (1968).

[11] J. Bailey *et al.* (CERN-Mainz-Daresbury Collaboration), Final report on the CERN muon storage ring including the anomalous magnetic moment and the electric dipole moment of the muon, and a direct test of relativistic time dilation, *Nuclear Physics B* **150**, 1 (1979).

[12] G. W. Bennett *et al.* (Muon $g - 2$ Collaboration), Final report of the muon E821 anomalous magnetic moment measurement at BNL, *Phys. Rev. D* **73**, 072003 (2006).

[13] B. Abi *et al.* (Muon $g - 2$ Collaboration), Measurement of the Positive Muon Anomalous Magnetic Moment to 0.46 ppm, *Phys. Rev. Lett.* **126**, 141801 (2021).

[14] D. P. Aguillard *et al.* (Muon $g - 2$), Measurement of the Positive Muon Anomalous Magnetic Moment to 0.20 ppm, *Phys. Rev. Lett.* **131**, 161802 (2023).

[15] J. Grange *et al.* (Muon $g - 2$ Collaboration), Muon $g - 2$ Technical Design Report (2015), arXiv:1501.06858.

[16] T. Albahri *et al.* (Muon $g - 2$ Collaboration), Measurement of the anomalous precession frequency of the muon in the Fermilab Muon $g - 2$ Experiment, *Phys. Rev. D* **103**, 072002 (2021).

[17] T. Albahri *et al.* (Muon $g - 2$ Collaboration), Magnetic-field measurement and analysis for the Muon $g - 2$ Experiment at Fermilab, *Phys. Rev. A* **103**, 042208 (2021).

[18] T. Albahri *et al.* (Muon $g - 2$ Collaboration), Beam dynamics corrections to the Run-1 measurement of the muon anomalous magnetic moment at Fermilab, *Phys. Rev. Accel. Beams* **24**, 044002 (2021).

[19] D. P. Aguillard *et al.* (Muon $g - 2$ Collaboration), Detailed Report on the Measurement of the Positive Muon Anomalous Magnetic Moment to 0.20 ppm, *Phys. Rev. D* **110**, 032009 (2024).

[20] G. T. Danby *et al.*, The Brookhaven muon storage ring magnet, *Nucl. Instrum. Methods Phys. Res., Sect. A* **457**, 151 (2001).

[21] A. P. Schreckenberger *et al.*, The fast non-ferric kicker system for the Muon $g - 2$ Experiment at Fermilab, *Nucl. Instrum. Methods Phys. Res., Sect. A* **1011**, 165597 (2021).

[22] Y. K. Semertzidis *et al.*, The Brookhaven muon ($g - 2$) storage ring high voltage quadrupoles, *Nucl. Instrum. Methods Phys. Res., Sect. A* **503**, 458 (2003).

[23] J. Kaspar *et al.*, Design and performance of SiPM-based readout of PbF₂ crystals for high-rate, precision timing applications, *J. Instrum.* **12** (01), P01009.

[24] K. Khaw *et al.*, Performance of the Muon $g - 2$ calorimeter and readout systems measured with test beam data, *Nucl. Instrum. Methods Phys. Res., Sect. A* **945**, 162558 (2019).

[25] A. Anastasi *et al.*, Electron beam test of key elements of the laser-based calibration system for the muon $g - 2$ experiment, *Nucl. Instrum. Methods Phys. Res., Sect. A* **842**, 86 (2017).

[26] A. Anastasi *et al.*, The laser-based gain monitoring system of the calorimeters in the Muon $g - 2$ experiment at Fermilab, *J. Instrum.* **14** (11), P11025.

[27] S. Corrodi, P. D. Lurgio, D. Flay, J. Grange, R. Hong, D. Kawall, M. Oberling, S. Ramachandran, and P. Winter, Design and performance of an in-vacuum, magnetic field mapping system for the Muon $g - 2$ Experiment, *J. Instrum.* **15**, P11008 (2020).

[28] D. Flay *et al.*, High-accuracy absolute magnetometry with application to the fermilab muon $g - 2$ experiment, *Journal of Instrumentation* **16** (12), P12041.

[29] E. Swanson, M. Fertl, A. Garcia, C. Helling, R. Ortez, R. Osofsky, D. Peterson, R. Reimann, M. Smith, and T. Van Wechel, The fixed probe storage ring magnetometer for the Muon $g - 2$ experiment at Fermi National Accelerator Laboratory, *Nuclear Instruments and Methods in Physics Research Section A: Accelerators, Spectrometers, Detectors and Associated Equipment* **1075**, 170338 (2025).

[30] B. T. King *et al.*, The straw tracking detector for the Fermilab Muon $g - 2$ Experiment, *J. Instrum.* **17**, P02035 (2022).

[31] O. Kim *et al.*, Reduction of coherent betatron oscillations in a muon $g - 2$ storage ring experiment using RF fields, *New Journal of Physics* **22**, 063002 (2020).

[32] P. J. Mohr, E. Tiesinga, D. B. Newell, and B. N. Taylor, *Codata Internationally Recommended 2022 Values of the Fundamental Physical Constants* (2024).

[33] G. W. Bennett *et al.* (Muon $g - 2$ Collaboration), Statistical equations and methods applied to the precision Muon $g - 2$ Experiment at BNL, *Nucl. Instrum. Methods Phys. Res., Sect. A* **579**, 1096 (2007).

[34] M. Farooq, T. Chupp, J. Grange, A. Tewsley-Booth, D. Flay, D. Kawall, N. Sachdeva, and P. Winter, Absolute magnetometry with ^3He , *Phys. Rev. Lett.* **124**, 223001 (2020).

[35] H. Yamaguchi *et al.*, Development of a CW-NMR Probe for Precise Measurement of Absolute Magnetic Field, *IEEE Transactions on Applied Superconductivity* **29**, 1 (2019).

[36] R. Aliberti *et al.*, The anomalous magnetic moment of the muon in the Standard Model: an update (2025), arXiv:2505.21476 [hep-ph].

[37] T. Aoyama, M. Hayakawa, T. Kinoshita, and M. Nio, Complete Tenth-Order QED Contribution to the Muon $g - 2$, *Phys. Rev. Lett.* **109**, 111808 (2012), arXiv:1205.5370 [hep-ph].

[38] S. Volkov, Calculating the five-loop QED contribution to the electron anomalous magnetic moment: Graphs without lepton loops, *Phys. Rev. D* **100**, 096004 (2019), arXiv:1909.08015 [hep-ph].

[39] S. Volkov, Calculation of the total 10th order QED contribution to the electron magnetic moment, *Phys. Rev. D* **110**, 036001 (2024), arXiv:2404.00649 [hep-ph].

[40] T. Aoyama, M. Hayakawa, A. Hirayama, and M. Nio, Verification of the tenth-order QED contribution to the anomalous magnetic moment of the electron from diagrams without fermion loops, *Phys. Rev. D* **111**, L031902 (2025), arXiv:2412.06473 [hep-ph].

[41] R. H. Parker, C. Yu, W. Zhong, B. Estey, and H. Müller, Measurement of the fine-structure constant as a test of the Standard Model, *Science* **360**, 191 (2018), arXiv:1812.04130 [physics.atom-ph].

[42] L. Morel, Z. Yao, P. Cladé, and S. Guellati-Khélifa, Determination of the fine-structure constant with an accuracy of 81 parts per trillion, *Nature* **588**, 61 (2020).

[43] A. Czarnecki, W. J. Marciano, and A. Vainshtein, Refinements in electroweak contributions to the muon anomalous magnetic moment, *Phys. Rev. D* **67**, 073006 (2003), [Erratum: *Phys. Rev. D* **73**, 119901 (2006)], arXiv:hep-ph/0212229 [hep-ph].

[44] C. Gnendiger, D. Stöckinger, and H. Stöckinger-Kim, The electroweak contributions to $(g - 2)_\mu$ after the Higgs boson mass measurement, *Phys. Rev. D* **88**, 053005 (2013), arXiv:1306.5546 [hep-ph].

[45] J. Lüdtke, M. Procura, and P. Stoffer, Dispersion relations for the hadronic VVA correlator, *JHEP* **04**, 130, arXiv:2410.11946 [hep-ph].

[46] M. Hoferichter, J. Lüdtke, L. Naterop, M. Procura, and P. Stoffer, Improved evaluation of the electroweak contribution to muon $g - 2$, *Phys. Rev. Lett.* **134**, 201801 (2025), arXiv:2503.04883 [hep-ph].

[47] T. Blum, P. A. Boyle, V. Gülpers, T. Izubuchi, L. Jin, C. Jung, A. Jüttner, C. Lehner, A. Portelli, and J. T. Tsang (RBC, UKQCD), Calculation of the hadronic vacuum polarization contribution to the muon anomalous magnetic moment, *Phys. Rev. Lett.* **121**, 022003 (2018), arXiv:1801.07224 [hep-lat].

[48] D. Giusti, V. Lubicz, G. Martinelli, F. Sanfilippo, and S. Simula (ETM), Electromagnetic and strong isospin-breaking corrections to the muon $g - 2$ from Lattice QCD+QED, *Phys. Rev. D* **99**, 114502 (2019), arXiv:1901.10462 [hep-lat].

[49] S. Borsányi *et al.*, Leading hadronic contribution to the muon magnetic moment from lattice QCD, *Nature* **593**, 51 (2021), arXiv:2002.12347 [hep-lat].

[50] C. Lehner and A. S. Meyer, Consistency of hadronic vacuum polarization between lattice QCD and the R-ratio, *Phys. Rev. D* **101**, 074515 (2020), arXiv:2003.04177 [hep-lat].

[51] G. Wang, T. Draper, K.-F. Liu, and Y.-B. Yang (χ QCD), Muon $g - 2$ with overlap valence fermions, *Phys. Rev. D* **107**, 034513 (2023), arXiv:2204.01280 [hep-lat].

[52] C. Aubin, T. Blum, M. Golterman, and S. Peris, Muon anomalous magnetic moment with staggered fermions: Is the lattice spacing small enough?, *Phys. Rev. D* **106**, 054503 (2022), arXiv:2204.12256 [hep-lat].

[53] M. Cè *et al.*, Window observable for the hadronic vacuum polarization contribution to the muon $g - 2$ from lattice QCD, *Phys. Rev. D* **106**, 114502 (2022), arXiv:2206.06582 [hep-lat].

[54] C. Alexandrou *et al.* (ETM), Lattice calculation of the short and intermediate time-distance hadronic vacuum polarization contributions to the muon magnetic moment using twisted-mass fermions, *Phys. Rev. D* **107**, 074506 (2023), arXiv:2206.15084 [hep-lat].

[55] T. Blum *et al.* (RBC, UKQCD), Update of Euclidean windows of the hadronic vacuum polarization, *Phys. Rev. D* **108**, 054507 (2023), arXiv:2301.08696 [hep-lat].

[56] S. Kuberski, M. Cè, G. von Hippel, H. B. Meyer, K. Ott nad, A. Risch, and H. Wittig, Hadronic vacuum polarization in the muon $g - 2$: the short-distance contribution from lattice QCD, *JHEP* **03**, 172, arXiv:2401.11895 [hep-lat].

[57] A. Boccaletti *et al.*, High precision calculation of the hadronic vacuum polarisation contribution to the muon anomaly (2024), arXiv:2407.10913 [hep-lat].

[58] S. Spiegel and C. Lehner, A high-precision continuum limit study of the HVP short-distance window (2024), accepted for publication in *Phys. Rev. D*, arXiv:2410.17053 [hep-lat].

[59] T. Blum *et al.* (RBC, UKQCD), The long-distance window of the hadronic vacuum polarization for the muon $g - 2$, *Phys. Rev. Lett.* **134**, 201901 (2025), arXiv:2410.20590 [hep-lat].

[60] D. Djukanovic, G. von Hippel, S. Kuberski, H. B. Meyer, N. Miller, K. Ott nad, J. Parrino, A. Risch, and H. Wittig, The hadronic vacuum polarization contribution to the muon $g - 2$ at long distances, *JHEP* **04**, 098, arXiv:2411.07969 [hep-lat].

[61] C. Alexandrou *et al.* (ETM), Strange and charm quark contributions to the muon anomalous magnetic moment in lattice QCD with twisted-mass fermions, *Phys. Rev. D* **111**, 054502 (2025), arXiv:2411.08852 [hep-lat].

[62] A. Bazavov *et al.* (Fermilab Lattice, HPQCD, MILC), Hadronic vacuum polarization for the muon $g - 2$ from lattice QCD: Complete short and intermediate windows, *Phys. Rev. D* **111**, 094508 (2025), arXiv:2411.09656 [hep-lat].

[63] A. Bazavov *et al.*, Hadronic vacuum polarization for the muon $g - 2$ from lattice QCD: Long-distance and full light-quark connected contribution (2024), accepted for publication in *Phys. Rev. Lett.*, arXiv:2412.18491 [hep-lat].

[64] A. Keshavarzi, D. Nomura, and T. Teubner, The $g - 2$ of charged leptons, $\alpha(M_Z^2)$ and the hyperfine splitting of muonium, *Phys. Rev. D* **101**, 014029 (2020), arXiv:1911.00367 [hep-ph].

[65] L. Di Luzio, A. Keshavarzi, A. Masiero, and P. Paradisi, Model-Independent Tests of the Hadronic Vacuum Polarization Contribution to the Muon $g - 2$, *Phys. Rev. Lett.* **134**, 011902 (2025), arXiv:2408.01123 [hep-ph].

[66] A. Kurz, T. Liu, P. Marquard, and M. Steinhauser, Hadronic contribution to the muon anomalous magnetic

moment to next-to-next-to-leading order, *Phys. Lett. B* **734**, 144 (2014), arXiv:1403.6400 [hep-ph].

[67] G. Colangelo, M. Hoferichter, M. Procura, and P. Stoffer, Dispersion relation for hadronic light-by-light scattering: theoretical foundations, *JHEP* **09**, 074, arXiv:1506.01386 [hep-ph].

[68] P. Masjuan and P. Sánchez-Puertas, Pseudoscalar-pole contribution to the $(g_\mu - 2)$: a rational approach, *Phys. Rev. D* **95**, 054026 (2017), arXiv:1701.05829 [hep-ph].

[69] G. Colangelo, M. Hoferichter, M. Procura, and P. Stoffer, Dispersion relation for hadronic light-by-light scattering: two-pion contributions, *JHEP* **04**, 161, arXiv:1702.07347 [hep-ph].

[70] M. Hoferichter, B.-L. Hoid, B. Kubis, S. Leupold, and S. P. Schneider, Dispersion relation for hadronic light-by-light scattering: pion pole, *JHEP* **10**, 141, arXiv:1808.04823 [hep-ph].

[71] G. Eichmann, C. S. Fischer, E. Weil, and R. Williams, Single pseudoscalar meson pole and pion box contributions to the anomalous magnetic moment of the muon, *Phys. Lett. B* **797**, 134855 (2019), [Erratum: *Phys. Lett. B* **799**, 135029 (2019)], arXiv:1903.10844 [hep-ph].

[72] J. Bijnens, N. Hermansson-Truedsson, and A. Rodríguez-Sánchez, Short-distance constraints for the HLbL contribution to the muon anomalous magnetic moment, *Phys. Lett. B* **798**, 134994 (2019), arXiv:1908.03331 [hep-ph].

[73] J. Leutgeb and A. Rebhan, Axial vector transition form factors in holographic QCD and their contribution to the anomalous magnetic moment of the muon, *Phys. Rev. D* **101**, 114015 (2020), arXiv:1912.01596 [hep-ph].

[74] L. Cappiello, O. Catà, G. D'Ambrosio, D. Greynat, and A. Iyer, Axial-vector and pseudoscalar mesons in the hadronic light-by-light contribution to the muon $(g - 2)$, *Phys. Rev. D* **102**, 016009 (2020), arXiv:1912.02779 [hep-ph].

[75] P. Masjuan, P. Roig, and P. Sánchez-Puertas, The interplay of transverse degrees of freedom and axial-vector mesons with short-distance constraints in $g - 2$, *J. Phys. G* **49**, 015002 (2022), arXiv:2005.11761 [hep-ph].

[76] J. Bijnens, N. Hermansson-Truedsson, L. Laub, and A. Rodríguez-Sánchez, Short-distance HLbL contributions to the muon anomalous magnetic moment beyond perturbation theory, *JHEP* **10**, 203, arXiv:2008.13487 [hep-ph].

[77] J. Bijnens, N. Hermansson-Truedsson, L. Laub, and A. Rodríguez-Sánchez, The two-loop perturbative correction to the $(g - 2)_\mu$ HLbL at short distances, *JHEP* **04**, 240, arXiv:2101.09169 [hep-ph].

[78] I. Danilkin, M. Hoferichter, and P. Stoffer, A dispersive estimate of scalar contributions to hadronic light-by-light scattering, *Phys. Lett. B* **820**, 136502 (2021), arXiv:2105.01666 [hep-ph].

[79] D. Stamen, D. Hariharan, M. Hoferichter, B. Kubis, and P. Stoffer, Kaon electromagnetic form factors in dispersion theory, *Eur. Phys. J. C* **82**, 432 (2022), arXiv:2202.11106 [hep-ph].

[80] J. Leutgeb, J. Mager, and A. Rebhan, Hadronic light-by-light contribution to the muon $g - 2$ from holographic QCD with solved $U(1)_A$ problem, *Phys. Rev. D* **107**, 054021 (2023), arXiv:2211.16562 [hep-ph].

[81] M. Hoferichter, B. Kubis, and M. Zanke, Axial-vector transition form factors and $e^+e^- \rightarrow f_1\pi^+\pi^-$, *JHEP* **08**, 209, arXiv:2307.14413 [hep-ph].

[82] M. Hoferichter, P. Stoffer, and M. Zillinger, An optimized basis for hadronic light-by-light scattering, *JHEP* **04**, 092, arXiv:2402.14060 [hep-ph].

[83] E. J. Estrada, S. González-Solís, A. Guevara, and P. Roig, Improved π^0, η, η' transition form factors in resonance chiral theory and their a_μ^{HLbL} contribution, *JHEP* **12**, 203, arXiv:2409.10503 [hep-ph].

[84] O. Deineka, I. Danilkin, and M. Vanderhaeghen, Dispersive estimate of the $a_0(980)$ contribution to $(g-2)_\mu$, *Phys. Rev. D* **111**, 034009 (2025), arXiv:2410.12894 [hep-ph].

[85] G. Eichmann, C. S. Fischer, T. Haeuser, and O. Regenfelder, Axial-vector and scalar contributions to hadronic light-by-light scattering, *Eur. Phys. J. C* **85**, 445 (2025), arXiv:2411.05652 [hep-ph].

[86] J. Bijnens, N. Hermansson-Truedsson, and A. Rodríguez-Sánchez, Constraints on the hadronic light-by-light tensor in corner kinematics for the muon $g - 2$, *JHEP* **03**, 094, arXiv:2411.09578 [hep-ph].

[87] M. Hoferichter, P. Stoffer, and M. Zillinger, Dispersion relation for hadronic light-by-light scattering: subleading contributions, *JHEP* **02**, 121, arXiv:2412.00178 [hep-ph].

[88] S. Holz, M. Hoferichter, B.-L. Hoid, and B. Kubis, Dispersion relation for hadronic light-by-light scattering: η and η' poles, *JHEP* **04**, 147, arXiv:2412.16281 [hep-ph].

[89] L. Cappiello, J. Leutgeb, J. Mager, and A. Rebhan, Tensor meson transition form factors in holographic QCD and the muon $g - 2$ (2025), arXiv:2501.09699 [hep-ph].

[90] G. Colangelo, M. Hoferichter, A. Nyffeler, M. Passera, and P. Stoffer, Remarks on higher-order hadronic corrections to the muon $g - 2$, *Phys. Lett. B* **735**, 90 (2014).

[91] T. Blum, N. Christ, M. Hayakawa, T. Izubuchi, L. Jin, C. Jung, and C. Lehner, The hadronic light-by-light scattering contribution to the muon anomalous magnetic moment from lattice QCD, *Phys. Rev. Lett.* **124**, 132002 (2020), arXiv:1911.08123 [hep-lat].

[92] E.-H. Chao, R. J. Hudspith, A. Gérardin, J. R. Green, H. B. Meyer, and K. Ottnad, Hadronic light-by-light contribution to $(g - 2)_\mu$ from lattice QCD: a complete calculation, *Eur. Phys. J. C* **81**, 651 (2021), arXiv:2104.02632 [hep-lat].

[93] E.-H. Chao, R. J. Hudspith, A. Gérardin, J. R. Green, and H. B. Meyer, The charm-quark contribution to light-by-light scattering in the muon $(g - 2)$ from lattice QCD, *Eur. Phys. J. C* **82**, 664 (2022), arXiv:2204.08844 [hep-lat].

[94] T. Blum, N. Christ, M. Hayakawa, T. Izubuchi, L. Jin, C. Jung, C. Lehner, and C. Tu (RBC, UKQCD), Hadronic light-by-light contribution to the muon anomaly from lattice QCD with infinite volume QED at physical pion mass, *Phys. Rev. D* **111**, 014501 (2025), arXiv:2304.04423 [hep-lat].

[95] Z. Fodor, A. Gérardin, L. Lellouch, K. K. Szabó, B. C. Toth, and C. Zimmermann, Hadronic light-by-light scattering contribution to the anomalous magnetic moment of the muon at the physical pion mass (2024), accepted for publication in *Phys. Rev. D*, arXiv:2411.11719 [hep-lat].

[96] T. Aoyama *et al.*, The anomalous magnetic moment of the muon in the Standard Model, *Phys. Rep.* **887**, 1 (2020).

[97] F. V. Ignatov *et al.* (CMD-3 Collaboration), Measurement of the $e^+e^- \rightarrow \pi^+\pi^-$ cross section from threshold to 1.2 GeV with the CMD-3 detector, *Phys. Rev. D* **109**, 112002 (2024).

[98] F. V. Ignatov *et al.* (CMD-3 Collaboration), Measure-

ment of the Pion Form Factor with CMD-3 Detector and

Its Implication to the Hadronic Contribution to Muon
 $(g - 2)$, *Phys. Rev. Lett.* **132**, 231903 (2024).

Measurement of the Positive Muon Anomalous Magnetic Moment to 127 ppb

Supplemental Material

We present additional information for the final measurement of the muon magnetic anomaly, a_μ , by the Muon $g-2$ Experiment at Fermi National Accelerator Laboratory. Five sections provide background on the run history, a new radio frequency (RF) system, the fit functions for the extraction of ω_a , a residual gain correction, and our improved understanding of the differential decay correction. A forthcoming publication will further detail the analysis and improvements over our earlier publications.

Run history — The Muon $g-2$ Experiment collected data over six physics runs, summarized in Table I, from 2018 to 2023, with improved operational stability achieved in the later periods. Run-1 (2018), the first physics run, had variable operational parameters, including kicker voltages ranging from 125 kV–137 kV and electrostatic quadrupole (ESQ) performance variations due to damaged high-voltage resistors, which were identified and replaced after the run. During Run-2/3 (2019–2020) the experiment’s temperature stability improved, kicker upgrades enabled better beam centering, and the ESQ voltage optimization minimized resonances and reduced muon losses. The final three runs, the focus of this publication, Run-4/5/6, operated under largely consistent conditions, with its primary distinction being the staged introduction of RF modulation to the ESQ system to reduce coherent betatron oscillation (CBO) amplitudes.

RF system — The ESQ RF system applied a ~ 1 kV RF voltage modulation tuned to the CBO frequency during the first $6\ \mu\text{s}$ after beam injection, which resonantly damped the coherent beam motion by more than a factor of five, significantly reducing its impact on ω_a^m . Omission of the CBO-related terms from the ω_a fits shifts ω_a by 0.8 ppm in data without the RF but only by 0.1 ppm with the RF. While the dominant CBO systematic uncertainty, stemming from limited knowledge of its decoherence behavior, remained similar between datasets, the consistent ω_a^m values obtained with and without RF bolsters confidence in the robustness of the CBO treatment.

The RF field also helped center the stored beam by rebalancing the phase-space distribution of high- and low-momentum muons, thereby reducing the electric field correction C_e as follows. Underkicking by the kicker causes the stored muons to oscillate with large CBO amplitude. In the absence of RF, high-momentum muons, which are initially closer to the ideal orbit, receive a kick closer to optimal and thus remain nearer the ideal orbit, while low-momentum muons get pushed further from equilibrium. As a result, more high-momentum muons survive post-kick, shifting the beam centroid. The RF acts to bring low-momentum muons closer to the ideal orbit

while pushing high-momentum muons away, making their motion out of phase but matched in amplitude and population. This centering of the beam reduces both C_e and muon loss during storage, and thus improves the overall quality and stability of the stored beam. *Fit function details* — The transverse oscillations of the muon beam and the spread of muon momenta introduce complexity into the precession data, which the terms $\eta_N(t)$, $\eta_A(t)$ and $\eta_\phi(t)$ capture in the fit model

$$N(t) = N_0 \Lambda(t) \eta_N(t) e^{-t/\gamma\tau_\mu} \times \{1 + A \eta_A(t) \cos [\omega_a^m t - \varphi_0 + \eta_\phi(t)]\}. \quad (1)$$

The oscillations couple to the variation of positron acceptance with muon decay position. For example, the normalization modulation takes the form

$$\eta_N(t) = X(t) + Y(t) + XY(t), \quad (2)$$

where $X(t) = \sum A_i(t) \cos(\omega_i t + \phi_i(t))$ arises from the coupling of the horizontal beam oscillations with horizontal acceptance. A similar form for $Y(t)$ arises from the vertical oscillation and acceptance, while $XY(t)$ mixes horizontal and vertical frequencies because of the variation of the vertical acceptance function with horizontal position. Nonlinearities in the ESQ fields cause a slow drift in the muon ensemble-averaged betatron frequencies over the course of a muon fill which the time dependence in $\phi_i(t)$ captures. The relative amplitudes of the betatron frequencies are well understood. The dominantly linear horizontal and quadratic vertical acceptances cause the horizontal betatron frequency, aliased to f_{CBO} and the second harmonic of the vertical frequency, aliased to f_{vw} to dominate. The acceptance modulation also results in modulation of the positron spectrum, which in turn modulates both the muon ensemble-averaged asymmetry A and precession phase ϕ . The correction terms $\eta_A(t)$ and $\eta_\phi(t)$ have forms similar to the $X(t)$ terms.

The five different analyses take a broad range of approaches for incorporating the time dependence of the envelopes $A_i(t)$ or $\alpha_i(t)$ and $\beta_i(t)$, which eventually decay away as the beam oscillations decohere. The approaches range from purely analytical forms with parameters floating in the fit to data-driven forms where the amplitudes are measured in time bins and then smoothed. *Residual gain correction* — The initial flash of beam particles at injection causes a gain sag in the calorimeters as capacitors are depleted and bias voltages recover. The laser system [1] measures this effect *in-situ* and provides gain corrections that are exponential with $\mathcal{O}(6\ \mu\text{s})$ time constants governed by the capacitance of the detector electronics [2, 3]. Short term — $\mathcal{O}(10\ \text{ns})$ — effects from the

Dataset	ESQ (kV)	RF mode	Kicker (kV)	Field index	Positrons (10^9)	Mag. Field Maps
Run-1	18.3	—	125 to 137	0.107 to 0.120	15.4	16
Run-2/3	18.2	—	142 and 161	0.107 to 0.108	70.9	69
noRF	18.2	—	161	0.108	86.0	71
xRF	18.2	x	161	0.108	49.3	40
xyRF5	18.2	xy	161	0.108	47.8	37
xyRF6	18.2	xy	161	0.108	39.1	46

TABLE I. Key parameters for the Muon g-2 dataset periods. The RF mode indicates which ESQ RF components were used: no RF (—), horizontal only (x), or both horizontal and vertical (xy), the field index n , the number of analyzed positrons within the energy range 1 GeV/c–3.1 GeV/c detected more than 30 μ s after the muon injection, and the number of magnetic field maps.

recovery of individual silicon photomultiplier pixels from single positron hits are also corrected.

Each shower also causes a small gain sag with the $\mathcal{O}(6 \mu\text{s})$ time constant. This effect and its scaling with the number of photoelectrons was confirmed with dedicated measurements of a modified calorimeter station after the completion of Run-6. These small gain perturbations build up iteratively over a muon fill and distort the exponential flash recovery. The distortion due to this effect was considered during design of the calorimeter electronics [4] and is visible in the residuals of laser monitor data after the correction for the flash. The relative amplitude of this effect is below our design goal of $< 10^{-4}$ at 30 μs , so no correction was calculated for previous publications.

Because the amplitude of the gain sag is proportional to the deposited energy and the recovery time constant is about the ω_a period, the oscillation of the average positron energy in the detectors imprints a phase-shifted ω_a oscillation onto the gain correction. This phase shift leads to a bias in ω_a^m much larger than an exponential or in-phase oscillating gain sag if not corrected. With the Run-4/5/6 beam rates, this gain sag caused a shift of 40 ppb in ω_a^m with an amplitude below the design sensitivity of our laser monitoring system.

Differential decay — The differential decay correction

$$C_{dd} = \left(\frac{1}{\omega_a} \right) \left(\frac{d\varphi_0}{dp} \right) \left(\frac{dp}{dt} \right)_{dd} \quad (3)$$

to ω_a^m arises from correlations between the initial phase of the spin precession after injection and the momentum of stored muons. The coupling of this correlation and the evolving momentum distribution due to the momentum-dependent muon lifetime leads to a temporal evolution of the ensemble-averaged initial phase, φ_0 , which in turn shifts the measured spin precession frequency.

We directly calculate the time evolution of the momentum spread from its width σ_p , i.e.,

$$\left(\frac{dp}{dt} \right)_{dd} \approx \frac{1}{\bar{p}\gamma\tau_\mu} \sigma_p^2, \quad (4)$$

with \bar{p} the mean momentum. The momentum-phase correlation $d\varphi_0/dp$ can be decomposed into two parts: the *injection* and *longitudinal* components.

The *injection* component emerges from initial phase correlations with muon momentum and transverse phase space coordinates that originate from the muon production, transport to the experiment, and injection into the storage ring. We extract this component from high-fidelity simulations that reproduce the effects of pion decay and muon momentum on the spin phase advance, as well as the correlations at injection time between the radial phase space coordinates and momentum for muons that store. Since all these aspects define the injection component, we cover a wide range of configurations that lead to a contribution $C_{dd}(\text{Injection})$ of 19–20 ppb with a conservative uncertainty estimate of 20 ppb.

The *longitudinal* component arises from the dependence of momentum acceptance on the longitudinal coordinate within the stored muon bunch. The temporal shape of the kicker pulse determines this effect. This correspondence between momentum and muon time-of-flight accentuates the muon spin-precession gradient from the head to the tail of the stored beam, which together yield $C_{dd}(\text{Longitudinal})$ of 4–8 ppb with uncertainties of 17–19 ppb. The total correction is $C_{dd} = 26 \pm 27$ ppb.

- [1] A. Anastasi *et al.*, The laser-based gain monitoring system of the calorimeters in the Muon g-2 experiment at Fermilab, *J. Instrum.* **14** (11), P11025.
- [2] T. Albahri *et al.* (Muon $g - 2$ Collaboration), Measurement of the anomalous precession frequency of the muon in the Fermilab Muon $g - 2$ Experiment, *Phys. Rev. D* **103**, 072002 (2021).
- [3] D. P. Aguillard *et al.* (Muon $g - 2$ Collaboration), Detailed Report on the Measurement of the Positive Muon Anomalous Magnetic Moment to 0.20 ppm, *Phys. Rev. D* **110**, 032009 (2024).
- [4] J. Kaspar *et al.*, Design and performance of SiPM-based readout of PbF₂ crystals for high-rate, precision timing applications, *J. Instrum.* **12** (01), P01009.